

Crystalline, Phononic and Electronic properties of Heterostructured Polytypic Ge Nanowires by Raman Spectroscopy

Claudia Fasolato^{†}⊥, Marta De Luca[†], Doriane Djomani[§], Laetitia Vincent[§], Charles Renard[§],
Giulia Di Iorio[†], Vincent Paillard[¥], Michele Amato[#], Riccardo Rurali[‡], and Ilaria Zardo^{†*}.*

[†]Departement Physik, Universität Basel, Klingelbergstrasse 82, 4056 Basel, Switzerland

[§]Centre de Nanosciences et Nanotechnologies (C2N), CNRS, Univ. Paris-Sud, Université
Paris-Saclay, Bât 220, rue André Ampère, Centre scientifique d'Orsay, F91405 Orsay
cedex, France

[¥]CEMES, University of Toulouse, CNRS, Toulouse, France

[#]Laboratoire de Physique des Solides (LPS), CNRS, Univ. Paris-Sud, Université Paris-Saclay,
Centre scientifique d'Orsay, F-91405 Orsay cedex, France

[‡]Institut de Ciència de Materials de Barcelona (ICMAB–CSIC), Campus de Bellaterra, 08193
Bellaterra, Barcelona, Spain

KEYWORDS. Heterostructure; nanowires; allotrope; Raman spectroscopy; phonons; electronic band alignment.

ABSTRACT Semiconducting nanowires (NWs) offer the unprecedented opportunity to host different crystal phases in a nanostructure, which enables the formation of polytypic heterostructures where the material composition is unchanged. This characteristic boosts the potential of polytypic heterostructured NWs for optoelectronic and phononic applications. In this work, we investigate cubic Ge NWs where small (~ 20 nm) hexagonal domains are formed due to a strain-induced phase transformation. By combining a non-destructive optical technique (Raman spectroscopy) with density-functional theory (DFT) calculations, we assess the phonon properties of hexagonal Ge, determine the crystal phase variations along the NW axis and, quite remarkably, reconstruct the relative orientation of the two polytypes. Moreover, we provide information on the electronic band alignment of the heterostructure at points of the Brillouin zone different from the one (Γ) where the direct band gap recombination in hexagonal Ge takes place. We demonstrate the versatility of Raman spectroscopy and show that it can be used to determine the main crystalline, phononic, and electronic properties of the most challenging type of heterostructure (a polytypic, nanoscale heterostructure with constant material composition). The general procedure that we establish can be applied to several types of heterostructures.

TEXT. When semiconductors are grown in the form of nanowires (NWs) they can exist in different crystal structures: this exciting phenomenon is known as polytypism.¹ NWs also allow for the existence of crystal phases that do not even exist in the bulk counterpart.^{2,3} Besides non-

nitride III-V materials, Si^{4,5,6,7,8,9} and Ge^{10,11,12} in the NW form can exist in the hexagonal 2H phase (properly named as lonsdaleite), which in the bulk is hardly obtained (usually under high pressure conditions).^{13,14}

The formation of NWs with hexagonal crystal symmetry has attracted enormous interest among researchers. Indeed, on one hand it allows some indirect band gap materials, such as Ge¹⁵ and Si_{1-x}Ge_x alloys,¹⁶ to feature a direct band gap,¹⁷ thus holding the promise for the realization of efficient and cost-effective optoelectronic Si-based devices.¹⁸ On the other hand, in III-V semiconductor NWs it has enabled the unprecedented possibility to switch between different crystal structures during the NW accretion, thus making crystal phase engineering a novel and powerful degree of freedom in the formation of heterostructures.^{19,20} In heterostructures, the electronic and phononic properties can be modulated along the NW axis, with enormous potential for optoelectronic,²¹ photovoltaics^{22,23} and thermoelectric^{24,25} applications. In the case of crystal-phase heterostructures, the further advantage is the absence of compositional disorder, which can result in defect-free abrupt interfaces.^{19,26}

Despite this great potential, the use of NWs embedding crystal-phase heterostructures is still quite limited. The main reason for that, along with the challenges involved in the NW growth, is the lack of a deep knowledge of their fundamental properties – especially for group IV semiconductor NWs. The *structural properties* that are important to assess in order to fully exploit a polytypic heterostructure are the nature of the crystal phases and their relative orientation. This information is usually obtained by transmission electron microscopy studies, which is however an invasive technique.¹⁰ As for the *electronic properties* of heterostructured NWs, the band gaps of the materials in the two crystal phases as well as the electronic band alignment are the crucial information to gain.^{27,28} Band gaps and band alignment can be probed with photoluminescence

and absorption studies, which have proved to be non-trivial (both in terms of experiment and interpretation) in NWs involving crystal structures not existing in the bulk.^{29,30} The case of hexagonal Ge, Si, and SiGe seems to be particularly challenging, as so far the optical studies are only theoretical,¹⁶ despite the availability of high quality NW samples.^{10,31,32,33} Moreover, the information on the band alignment in crystal-phase heterostructures that emission and absorption spectroscopies would provide is restricted to the point of the Brillouin zone where radiative recombination takes place (usually at Γ). For applications related to heat transport and management, the *phononic properties* of the material in the two crystal phases play a crucial role. These are usually investigated by resorting to Raman spectroscopy.^{34,35} Raman studies can be challenging in terms of interpretation, especially if the least known material (like the hexagonal phase in this study) is present in the heterostructure in a small volume fraction compared to the whole (cubic) NW, thus giving rise to small signals. This is especially the case of Ge, where, at variance with Si³¹ and SiGe³², the formation of hexagonal phase is difficultly achieved and it is often limited to small domains in the NW.^{10,28}

We present here a complete method able to fully address structural, electronic, and phononic properties of nanoscale heterostructures involving primarily a non-destructive experimental technique (Raman spectroscopy), coupled to theoretical (DFT) calculations. Raman spectroscopy is a broadly used technique to investigate many properties of NWs, such as the crystal composition, crystal phase, and strain level.^{34,35} In particular, *polarized Raman spectroscopy* in NWs has been employed for many different purposes. Ruling out the initial skepticism, indeed, over the last ten years Raman scattering studies on single NWs have proved that polarized Raman selection rules can be verified and observed experimentally even in nanoscale materials.^{36,37,38} Notably, in the case of hexagonal crystal, the azimuthal dependence of the E_{2g} mode on light polarization can

often be the killing proof in discriminating crystal domains from amorphous defects, as demonstrated in the case of hexagonal silicon.^{4,31,39,40} Besides the polarized Raman scattering, also *resonant Raman scattering (RRS)* has provided important insights in the NW properties. In particular, it has granted access to the electronic properties of NWs and to their modifications upon structural changes.^{41,42,43} RRS can allow assessing the energy gap of materials that exhibit an indirect bandgap,⁴⁴ energy gaps at different symmetry points than the Γ ,^{42,45} or the new permitted electronic transitions in a heterostructure.^{46,47} RRS also allows to detect the signal of a resonant small volume from a non-resonant large volume.^{48,49,50} In this work, we make a step forward in the use of Raman spectroscopy in NWs investigating a polytypic heterostructure in Ge NWs where small hexagonal domains are formed in the bottom part of NWs owing to a strain-induced phase transformation, described in Ref. 10. In particular, *i*) we assess for the first time the phonon modes of hexagonal Ge by combining Raman spectroscopy and density-functional theory (DFT) calculations; *ii*) we reconstruct the structural properties of the heterostructured NWs (both the crystal phase variations along the NW axis and the relative orientation of the two polytypes) by using spatially-resolved, polarized Raman spectroscopy giving access to selection rules; *iii*) we provide information on the electronic band alignment at L/M points by combining RRS and DFT calculations. We explain in detail the powerful and comprehensive approach we developed such that it can be generalized to investigate the main properties of different types of heterostructured NWs.

RESULTS AND DISCUSSION. We obtained hexagonal Ge by applying a strain-induced martensitic phase transformation to cubic Ge NWs (See Methods) resulting in a heterostructure with quasiperiodic embedded 2H-Ge nano-domains eventually distributed along the whole NW,

as detailed in Ref. 10. The Ge NWs investigated here were about 50 nm in diameter and 2.0-3.0 μm and have been transformed only partially and therefore consist of a heterostructured part of about 0.5-1 μm and an untransformed part of 1.5-2.5 μm . The length of the transformed segment at the basis of the NW can be tuned by controlling the height of the polymeric resist used for the transformation. In Figure 1A, we report a scanning electron microscopy (SEM) image of a representative NW lying on a (111) silicon surface: the transformed part is clearly recognizable as a zig-zag segment at the bottom of the NW, which results slightly tapered, by approximately 15% over the micrometric NW length, while the gold droplet used as growth catalyst is visible on the top of the structure.

In Figure 1B, the experimental configuration is sketched. Diamond crystal phase NWs with a $\langle 11 - 1 \rangle$ (z') growth direction are known to form facets of the type $\langle -110 \rangle$ (x') and $\langle 112 \rangle$ (y').^{51,52} This x', y', z' NW internal reference system is crucial for the interpretation of polarized Raman scattering studies. In our case, the NW growth axis z' lies in the plane of the substrate. The NW could be also additionally rotated of an arbitrary angle θ about the z' axis, which would result in a different orientation of the facet exposed to the laser light (see the schematic S3 in the SI S.1). This would have clear consequences on the polarized Raman spectra, as will be discussed in the following.

In Figure 1C we report a high-angle annular dark-field scanning transmission electron microscopy (HAADF-STEM) image acquired on a NW obtained along the $\langle -110 \rangle_{3C}$ zone axis. It is well known,^{13,14} and has been demonstrated for this sample,¹⁰ that for this type of martensitic transformation of germanium from diamond to hexagonal structure we retrieve the following symmetry relations:

$$[-110]_{3C} \parallel [2 - 1 - 10]_{2H}$$

$$(110)_{3C} \parallel (0001)_{2H}$$

This implies that there is a well-determined relative orientation of the different crystalline domains in the heterostructured part of the NW: this is depicted in Figure 1D, where different colors refer to different crystal phases (as in panel B) and this convention is kept throughout the manuscript.

In Figure 2, we compare the calculated Raman spectra of germanium in diamond/hexagonal crystal phases with our experimental results. We describe the scattering geometry adopted following the Porto notation:⁵³ in brackets, from left to right, we indicate the direction of polarization of the incident and scattered photons; outside brackets, from left to right, the direction of the k vector of the incident and scattered photons. The theoretical Raman spectra were generated assuming for the Raman modes a Lorentzian lineshape with FWHM = 2 cm⁻¹ centered at the computed frequencies for the phonon modes at the Γ point of the Brillouin Zone (BZ).

The predicted scattered intensity was calculated based on the following reasoning. In general, polarized Raman selection rules can be calculated to predict the visibility and intensity of specific Raman bands depending on the mode symmetry and on the scattering geometry (related to the experimental conditions). The Raman intensity of a given vibrational mode is proportional to a matrix product between the incident and scattered photon polarization vectors ε_{inc} , ε_{scat} and the Raman susceptibility tensor R ⁵⁴

$$I_{Raman} \propto | \varepsilon_{inc} \cdot R \cdot \varepsilon_{scat} |^2 \quad [1]$$

Loudon provides the general form of the Raman tensors for the normal vibrational modes at the Γ point of the BZ for different crystal systems. While the form of the Raman tensors (particularly,

which terms in the matrix are non-zero) can be inferred by symmetry considerations, the numerical values of the matrix elements depend on the electronic polarizability of the material system considered. The Raman tensors are in general provided in the principal axis reference systems, while the direction of photon polarization is more conveniently expressed in relation to the sample physical orientation (*e.g.* with respect to the NW growth axis).^{36,37} In order to calculate the product in equation [1], we therefore need to express the Raman tensors in the NW reference system. Obviously, the scalar quantity calculated in equation [1] does not eventually depend on the reference system chosen for the calculation. Given that the phonon modes and their symmetry depend on the crystal structure, so do the selection rules. Therefore, the visibility and azimuthal dependence of the intensity of a Raman peak on the incident/scattered photon polarization can allow not only to assess the crystal phase(s) of a material, but also its (their relative) orientation(s). The predicted scattered intensity is calculated according to equation [1] from the calculated Raman tensors, suitably expressed in the NW basis (Figure 1D), convenient for comparison with experimental data. Further details on the calculations can be found in the Supporting Information S.1.

The theoretical expected spectrum of the pure cubic phase is displayed in panel A. In panels B and C, we report the spectra acquired in the $x'(z'z')\bar{x}'$ and $x'(y'y')\bar{x}'$ configurations on the cubic untransformed (“top”) part of the NW. As expected from diamond-type crystals, the main feature of the spectrum is a single peak ascribed to the degenerate F_{2g} optical mode of germanium, centered at 300.8 cm^{-1} (FWHM = 2.9 cm^{-1}). The $x'(y'y')\bar{x}'$ spectrum (panel C) shows a significant drop in the intensity with respect to the $x'(z'z')\bar{x}'$ spectrum (panel B): this cannot be justified quantitatively just by Raman selection rules, but can be explained by considering the effect of the dielectric mismatch.⁵⁵ A NW is a micrometric sized antenna,⁵⁶ therefore the absorption⁵⁷ and

scattering efficiency^{58,59,60} are very sensitive to light polarization, and usually result detrimental for light polarized across the longitudinal NW axis^{58,59,60} (see also Figure 4 and discussion). It is worth noticing that the experimental spectra were collected exciting the system with the 633 nm line of a HeNe laser, as discussed in the Methods. As we will show with the resonant Raman study (Figure 5 and discussion), the normalized intensity of the F_{2g} mode vs the $F_{2g}+E_{1g}+A_{1g}$ is in the same order of magnitude, therefore artifacts provided by different resonant conditions can be excluded.

To calculate the theoretical, expected spectrum for the heterostructured part of the NW, we have weighted the spectral contribution of cubic and hexagonal phases with a factor 0.65 and 0.35, respectively; that is, we have assumed that 2H domains represent about 35% of the NW in the transformed part within our scattering volume, as confirmed by transmission electron microscopy (TEM) investigations. The crystal phases are assumed to be relatively oriented as sketched in Figure 1D. The resulting spectrum is shown in panel 2D. Two Raman bands are clearly visible. The one at lower frequency (286.1 cm^{-1}) is ascribed to the doubly degenerate E_{2g} phonon. The band at higher frequency consists of the contribution of three modes, respectively centered at 297.4 , 297.7 and 298.5 cm^{-1} . These are not resolved in the plot due to the finite peak width (*i.e.* 2 cm^{-1}) set to simulate realistic spectra. Two of these modes are the A_{1g} and the doubly degenerate E_{1g} modes, that appear from the splitting of the longitudinal and transverse optical (LO and TO) modes in the hexagonal crystal. The third is the F_{2g} optical phonon of the cubic phase. The contribution to the computed Raman spectrum of the pure cubic and hexagonal phases, for reference, are displayed in panel A and G, respectively, for the two most significant scattering geometries for comparison with the experimental data. In panels E and F, we report the spectra acquired in $x'(z'z')\bar{x}'$ and $x'(y'y')\bar{x}'$ configurations on the transformed (“bottom”) part of the

NW. Here we can as well recognize two main bands: one is centered at 286.7 cm^{-1} (the full width at half maximum, FWHM, is 5.3 cm^{-1}), which can be ascribed to the E_{2g} mode; the other is centered at 300.9 cm^{-1} (FWHM = 3.5 cm^{-1}) and is ascribed to the E_{1g} , A_{1g} modes of the hexagonal phase and to the F_{2g} mode of the cubic domains. It is worth mentioning that the mode frequencies predicted by density-functional calculations are generally slightly lower than the ones revealed experimentally. Nevertheless, the relative positioning of the modes and their predicted intensity are a reliable reference.

Our spatial resolution is diffraction-limited to few hundred nanometers, therefore the signal we collect on the heterostructured part of the NW will contain a contribution from both the hexagonal and the cubic nanodomain. We can expect a predominance of one or the other spectral signatures depending on how much of each phase is occupying our scattering volume: for the theoretical spectra we have assumed a 35%-65% (2H-3C) composition, as suggested by electron microscopy (see Figure 1). Coherently, in panel H and I, we report the spectral contribution of the hexagonal phase, extracted from the experimental data in panels E and F by subtracting the 65% of the cubic contribution (panels B and C). This results in good agreement with the theoretical prediction, despite a slight mismatch in the relative intensity of the two spectral components. The effect of the subtraction for different relative phase composition is discussed in the Supporting Information S.2 (Figure S6). We stress here that for computing the theoretical Raman spectra we have assumed the crystal orientation depicted in Figure 1D, fixing the degree of freedom associated with the rotation about the NW axis ($\theta = 0^\circ$). In the real case, as mentioned, the NW might be rotated by a finite θ about its axis: this would result in a different visibility and relative intensity of the Raman modes in the experimental spectra. Indeed, different visibility of the phonon modes of the two phases can be obtained changing the scattering geometry, *i.e.* tilting the plane of the substrate as done for the

spectra reported in Figure S4 in the Supporting Information S.2. In comparing the experimental results acquired on the two NW ends, we record a slight increase of the FWHM of the high frequency band in the transformed part with respect to the cubic reference data. This, as well as the polarized Raman azimuthal dependencies discussed in the following, corroborate our $F_{2g} + E_{1g} + A_{1g}$ assignment.

In Figure 3, we have reported the Raman intensities measured varying over 360° the incident light polarization, while keeping fixed the polarization of the detected light, which is set either parallel (z' polarized detection) or perpendicular (y' polarized detection) to the NW axis, *i.e.* $\langle 11 - 1 \rangle_{3C}$. In panel A, we reported the azimuthal dependence of the F_{2g} mode of the cubic phase (collected from the “top” part of the NW) and in panels B and C the polar response of the $F_{2g}+E_{1g}+A_{1g}$ mode and of the E_{2g} modes (collected from the heterostructured “bottom” part of the NW), respectively. In order to perform a correct interpretation of the experimental data, we have compared them with theoretical azimuthal dependencies calculated from the Raman susceptibility tensors. These have been initially expressed in the NW x', y', z' basis (Figure 1D), and then further rotated about the z' axis of the optimal angle $\theta = 33^\circ$. It is important to stress here, that θ is the rotation angle about the $\langle 11 - 1 \rangle_{3C}$ axis of the NW and not the in-plane angle between the $\langle 11 - 1 \rangle_{3C}$ and $\langle 0001 \rangle_{2H}$ axes. This rotation implies that the $\langle 0001 \rangle_{2H}$ axis is tilted out of plane with respect to the plane of the substrate (Figure S3 in SI S.1). The reference system used for the calculations is therefore $x'', y'', z'' = z'$, obtained by rotation of the x', y', z' about z' . A detailed discussion about the crystal orientation determination can be found in the Supporting Information S.1. In comparing panels A and D, we notice again that the intensity of the y'' polarized detection experimental plot is smaller than expected. As mentioned, this effect is to be ascribed to the dielectric mismatch, which is found to be more pronounced on the top part of

the NW. Panel E is in optimal agreement with the corresponding experimental data (in B). The slight discrepancy between the theoretical and experimental polar plots of the E_{2g} mode (panels F and C) is to be ascribed to the experimental error induced by the higher frequency band: as clearly visible in the fitting (Figure 2), there is a partial superimposition of the experimental lineshapes of the two modes, and therefore the polar dependencies of the E_{2g} mode result a bit tilted towards the correspondent polar plots of the $F_{2g}+E_{1g}+A_{1g}$ mode. Remarkably, the agreement between the theoretical and experimental azimuthal dependencies can be obtained only for an angle between α between the $\langle 11 - 1 \rangle_{3C}$ and $\langle 0001 \rangle_{2H}$ axes of about 35° and a rotation θ about the $\langle 11 - 1 \rangle_{3C}$ of 33° . As a further proof, we have measured the Raman spectra of the NW in the parallel and crossed configurations with respect to the $\langle 0001 \rangle_{2H}$ axis of the hexagonal segments. This was done by tilting the substrate plane and the NW axis of -33° and -35° . As shown in figure S4 of the SI S.2, the E_{2g} mode visibility is increased in this yy configuration, while the mode results substantially forbidden, as expected by selection rules, in zz configuration. We have thus demonstrated that polarized Raman spectroscopy reproduces with high fidelity the azimuthal response expected from theoretical considerations based on TEM. We argue therefore that this type of investigation can be generalized to polycrystalline and/or polytypic heterostructured in which the crystal orientation of the different regions is unknown.

In Figure 4, we present the results of one-dimensional polarized Raman scans acquired along the NW length. The spatially resolved investigation allows to monitor the changes in the Raman spectrum as a function of the position on the NW and to clearly locate the transformed segment of the NW. This is evident by the appearance of the E_{2g} signature in the spectroscopic maps, reported in panel A for the two main scattering configurations. The spectroscopic result is in excellent agreement with SEM imaging (Figure 1A) with respect to the spatial extension of the

heterostructured part of the NW. In panel B, we report the intensity of the two bands as a function of the position for the two polarizations, as estimated by Lorentzian fitting of the spectra. Interestingly, the intensity detected for the $F_{2g}+E_{1g}+A_{1g}$ peak, while being almost constant over all the NW in $x'(z'z')\bar{x}'$ configuration, seems to be strongly dependent on the position in $x'(y'y')\bar{x}'$, increasing continuously from top to bottom. We argue in this respect the contribution of two effects, both diminishing the polarization dependent intensity difference on the bottom transformed part of the NW: (i) the slight (10-15%) tapering of the NW, which is thinner on the top part, can cause optical resonances in the absorption dependent on diameter and excitation wavelength;⁶¹ (ii) the coexistence of two crystal phases, *i.e.* two materials with a different dielectric constant and electronic bands symmetry, stacked in segments in the heterostructure can result in different coupling efficiency with light. We expect the scattering efficiency to be possibly enhanced in the transformed part also due to the surface roughness arising from the zig-zag morphology in the transformed end of the NW.⁶² Notably, the fitting demonstrates that the FWHM of the $F_{2g}+E_{1g}+A_{1g}$ peak, while being constant over the untransformed part of the wire, increases remarkably on the transformed region, as expected if considering the assignment to multiple modes, which cannot be resolved but are not expected to be degenerate (see Figure S5 in the SI S.2).

Finally, we investigated the effect of the polytypic heterostructuring on the electronic band structure by means of RRS. Besides giving access to the symmetry of the phonon modes, Raman can also be used to probe the electronic band structure and the electron-phonon interaction in semiconductors.⁶³ Namely, the scattering cross section, which is proportional to the probability per unit time for one-phonon Raman scattering, contains the electron-radiation and the electron-phonon interaction Hamiltonians, as well as electronic states for electron-hole pair.^{54,63}

Nevertheless, it is experimentally very improbable to access this information, due to summation over all the intermediate states, unless resonant conditions are used. In resonant conditions the excitation energy is tuned to be equal to electronic inter-band transitions, leading to resonant Raman.

A RRS study was performed by varying the exciting photon energy over the visible spectral range and measuring the untransformed and transformed regions of the NW. The results are reported in Figure 5. All the data have been acquired keeping the exciting power fixed and normalizing the Raman scattered intensity to the one detected under the same conditions on a reference, non-resonant CaF₂ sample. This normalization removes the ω^4 dependence of the scattered intensity on the exciting phonon energy, as well as the influence of the experimental setup efficiency. A peak in the trend of the Raman intensity as a function of the exciting photon energy therefore can identify an optically allowed electronic transition that enhances the Raman cross section. In panel A of Figure 5, we report the dependence on the exciting wavelength of the intensity of the F_{2g} mode in the untransformed region. The trend of the Raman intensity is peaked around 2.2 eV, suggesting a possible electronic resonance in this energy range. The result is compatible with the reports on bulk germanium that can be found in the literature,⁴⁵ describing an electronic $E_1 - E_1 + \Delta_1$ optical transition at the L point of the BZ, around 2.25 eV, as also confirmed by our hybrid functional DFT calculations of the band-structure of 3C Ge (Figure 5D).⁴⁵ For the description of the resonant Raman mechanism in 3C Ge and the discrepancy between the E_1 gap value and observed resonance please refer to Ref. 45. When moving to the heterostructured part (panels B and C), we observe a different behavior: even if the scale of the enhancement is smaller, the trend is here peaked at lower energies, clearly below 2.2 eV. This can be explained with a new electronic resonant transition arising from band alignment in the heterostructured part of the NW.

As reported in the Figure 5E, DFT calculations of the electronic band structure of hexagonal Ge, including spin-orbit coupling, provide a value of the E_1 of 2.61 eV at the M point (that is equivalent to the L point of the cubic BZ).⁶⁴ The mere presence of the hexagonal phase is therefore not sufficient to explain the experimental observation. However, we need to consider that in a heterostructure different types of band alignment can take place, giving rise to new electronic transitions; the results discussed above (see *e.g.* Figure 2) clearly showed that, when we study the transformed region, our scattering volume include both the cubic and the hexagonal phase. In our case the electronic structure calculations reveal that, while the band alignment between the cubic and the hexagonal bands at the Γ point is of type I (panel F, left side), at the M/L point it is of type II (panel F, right side), resulting in an allowed optical transition of 2.12 eV, which fits very well the experimental result.

CONCLUSIONS

We have investigated cubic Ge NWs containing small hexagonal 2H segments (~ 20 nm). Not only the coexistence of different crystal phases stacked in a NW can result in a different phononic landscape but also, as well known, heterostructuring is the main ingredient for electronic bandgap engineering. Therefore, we have determined both the phononic and electronic properties of these polytypic heterostructures. We have combined Raman spectroscopy with first-principles electronic structure calculations and demonstrated that, when appropriate physical considerations are made, polarized Raman scattering can grant access to structural information even in nanoscale polytypic domains. These small domains can be localized with a diffraction-limited spatial resolution owing to the fact that phonon modes of different crystal phases have different frequencies and selection rules, which can be calculated as we explained. To the best of our knowledge, this work is the first demonstration of the potentiality of Raman spectroscopy in giving access to the crystal phase

relative orientation and to electronic band alignment properties (*i.e.*, type of band discontinuity and relative conduction and valence bands offsets), in a polytypic, nanoscale heterostructure, and therefore can provide new avenues for an exhaustive investigation of heterostructures in NWs.

METHODS. Sample growth and preparation. <111>-oriented Ge NWs were grown by VLS process using gold catalyst. After growth, they were embedded in a hardening hydrogen silsesquioxane resist (HSQ) which is thermally polymerized at 550°C during 10 minutes to form silica. The densification at high temperature induces a phase transformation in the NWs. The overall process and subsequent nanostructuration of Ge NWs have been described in Ref. 10. HAADF STEM showed 2H hexagonal domains periodically produced along the NWs (in the embedded part) resulting in 3C/2H heterostructures.

Raman Scattering experiments. The NW is illuminated with a high numerical aperture (0.8) 100x objective, which allows a spatial resolution of about 500 nm in the spectroscopic investigation. The polarization of the incident laser light and of the outgoing scattered beam can be controlled and selected by means of polarization optics to form an arbitrary angle φ with the NW growth axis. For the polarized Raman study, the collected scattered light was polarized either along ($\varphi = 0^\circ$, $\varepsilon_{z \text{ det}}$) or across ($\varphi = 90^\circ$, $\varepsilon_{y \text{ det}}$) the NW growth axis, while the incident light polarization ε_{inc} was varied over 360°. The scattered light was collected by a T64000 triple spectrometer equipped with a 1,800 $\text{g}\cdot\text{mm}^{-1}$ grating and a liquid nitrogen-cooled multichannel CCD detector, providing a spectral resolution below 1 cm^{-1} for the excitation wavelength used in these experiments. Polarized Raman experiments were performed exciting the system with the 633 nm line of a HeNe laser. The RRS study was performed by varying the exciting laser energy over the whole visible spectrum by using, in addition to the HeNe source, various lines of an Ar^+Kr^+ laser. The incident power was kept below 160 μW in order to avoid heating or damaging effects.

In order to take into account the wavelength dependence of both the efficiency of the setup and the intensity of the Raman cross section, the spectra were normalized to the intensity of the Raman band of a reference CaF₂ sample.

Computational Methods. The Raman susceptibility tensors were calculated within density-functional perturbation theory (DFPT) from the third derivative of the total energy, twice with respect to the application of an electric field and once with respect to the phonon displacement coordinates, making use of the 2n+1 theorem⁶⁵ as implemented in the ABINIT code.^{66,67} Density functional theory (DFT) calculations of electronic band structure were performed with the VASP code⁶⁸ using a hybrid Heyd–Scuseria–Ernzerhof (HSE06) functional⁶⁹ by mixing the exact non-local Hartree-Fock exchange energy with the semi-local Generalized Gradient Approximation (GGA) exchange and correlation functional⁷⁰ to achieve an accurate description of band gaps in particular in the case of small- medium band gap semiconductors. Spin-orbit, which is important in Ge, was also included. Full details of the computational methods can be found in the Supporting Information.

FIGURES

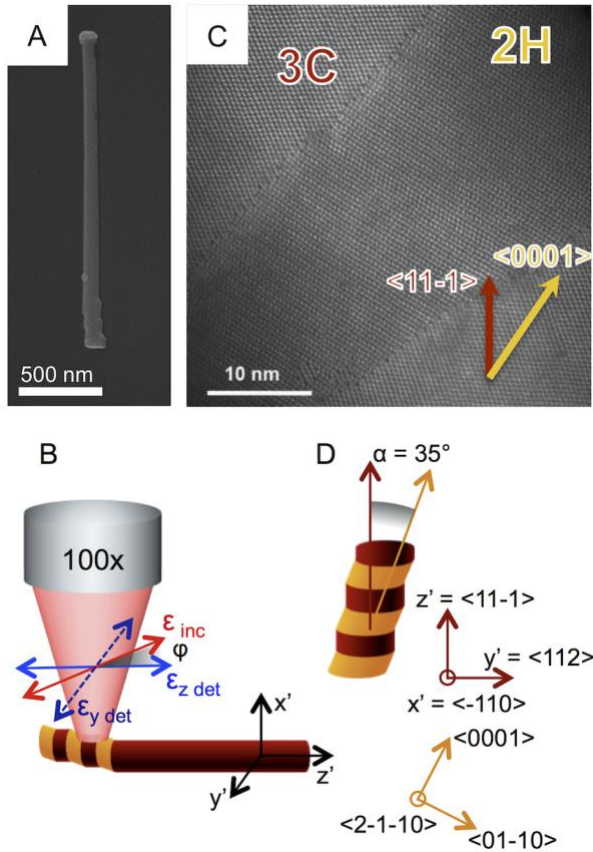


Figure 1. (A) SEM image of a Ge nanowire grown in the diamond phase. The gold particle is located on top of the wire, while the transformed heterostructured part (~ 300 nm long) is at the bottom. (B) Sketch of the experimental configuration: Raman scattering from the NW is collected in backscattering geometry by fixing the scattered light polarization either along ($\epsilon_{z\ det}$) or across ($\epsilon_{y\ det}$) the nanowire axis. A degree of indetermination is the angle of rotation of the nanowire about its growth axis (see S11). Different colors refer to different crystal phases and this convention it is kept throughout the entire manuscript. The schematic drawings are not to scale. (C) HAADF-STEM image of a hexagonal (2H) domain sandwiched between two diamond (3C) domains. The 2H (3C) domain is recognizable thanks to the ABABAB (ABCABC) stacking sequence. Image has been acquired from the crystalline $\langle -110 \rangle_{3C}$ direction, that is parallel to the $\langle 2 - 1 - 10 \rangle_{2H}$. The previously reported relation $(110)_{3C} // (0001)_{2H}$ is also verified.^{2,3} (D) Sketch of the crystal orientation of the 3C and 2H nano-domains in the heterostructured part of the NW.

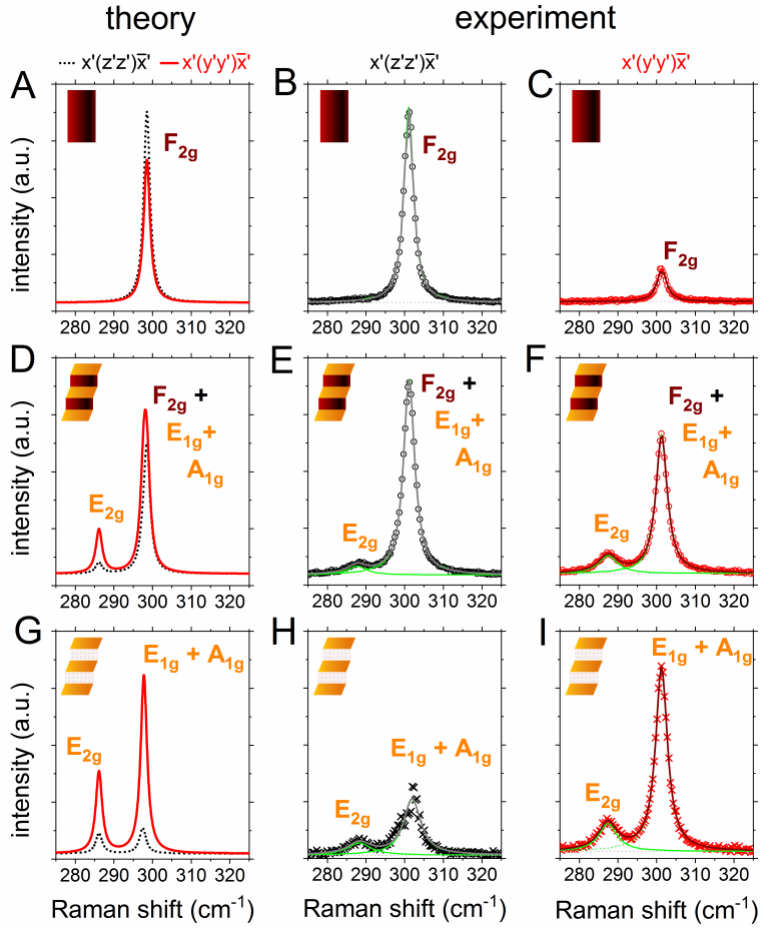


Figure 2. First row: cubic Ge. Panel A: theoretical Raman spectra, computed assuming a cubic Ge crystal oriented according to Figure 1D. The calculated spectrum well reproduces the experimental Raman data acquired on the untransformed part of the NW in the same $x'(z'z')\bar{x}'$ (panel B) and $x'(y'y')\bar{x}'$ (panel C) configurations (spectra are plotted with the same intensity scale; open circles are experimental data, gray/red solid line is the cumulative fitting). The lower intensity of the $x'(y'y')\bar{x}'$ spectrum displayed in panel C is to be ascribed to dielectric mismatch (see text). **Second row:** heterostructured part of Ge NW (color legend as in Figure 1). Panel D: calculated Raman spectra of heterostructured Ge, for $x'(z'z')\bar{x}'$ (black dashed line) and $x'(y'y')\bar{x}'$ (red solid line) scattering configurations. Theoretical spectra of pure cubic and hexagonal Ge, for reference, are plotted in panels A and G, respectively. In order to obtain the plots in D, the Raman spectra calculated for the two phases were weighted by a factor 0.35 (2H) and 0.65 (3C) and summed (orientation of the two phases as displayed in Fig. 1D was assumed). Lorentzian lineshapes with

FWHM = 2 cm⁻¹ are always adopted for the peaks ascribed to E_{2g}, and to F_{2g}, E_{1g} and A_{1g} modes: due to this choice (for a realistic comparison with experiments), the spectral resolution is not sufficient for resolving the three high frequency modes. The theoretical spectra well model the experimental data acquired on the transformed part of the NW, in $x'(z'z')\bar{x}'$ (panel E) and $x'(y'y')\bar{x}'$ (panel F) configurations (spectra are plotted with the same intensity scale; open circles are experimental data, gray/red solid line is the cumulative fitting, green solid lines highlight the different spectral components). **Third row:** hexagonal Ge. Panel G: computed spectra of pure hexagonal Ge oriented according to Figure 1D. E_{1g} and A_{1g} peaks appear as a unique peak due to the 2 cm⁻¹ FWHM. In panels H and I, we obtain the experimental 2H-Ge contribution (crosses) by subtracting to the experimental data in panels E and F the spectral contribution of the cubic phase (panels B and C, respectively) rescaled by a factor 0.65.

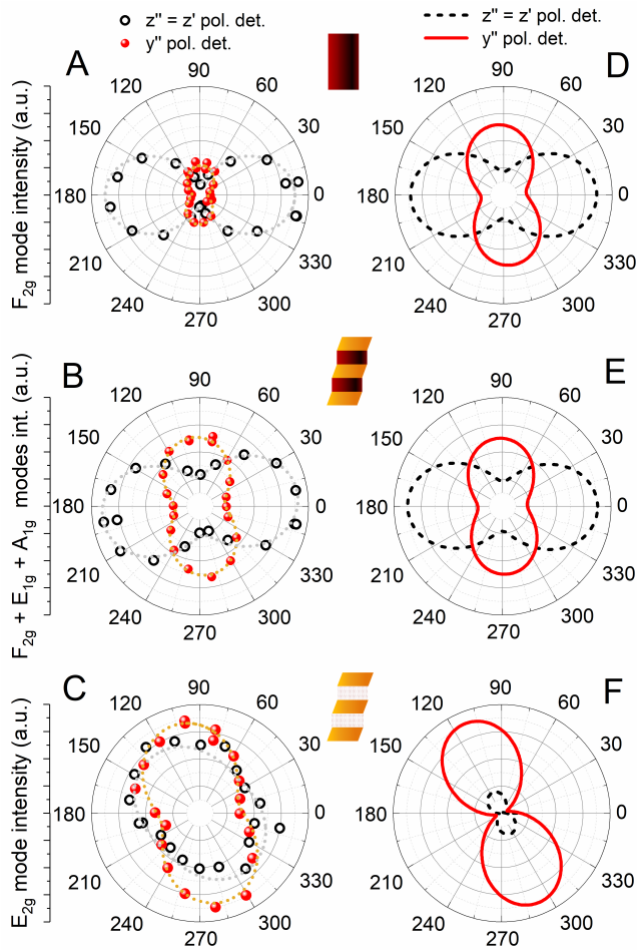


Figure 3. Left column, azimuthal dependencies on light polarization of the intensity of different Raman modes, obtained by collecting the scattered light polarized along (z'' detection, black empty circles) or across (y'' detection, red filled circles) the NW growth axis z' . The 0° corresponds to the z' direction. Dashed lines are cosine squared fits to the experimental data. Panel (A): F_{2g} mode of the diamond phase; panel (B): peak ascribed to convolution of F_{2g} mode of the 3C phase and to A_{1g} and E_{1g} modes of the 2H phase; panel (C): E_{2g} mode of the 2H phase. **Right column**, theoretical prediction for the same azimuthal dependencies considering the scattered light polarized along $z'' = z'$ (black dashed line) or along y'' (red solid line). These are obtained from the Raman tensors as described in the text, applying a rotation of $\theta = 33^\circ$ about the NW axis z' .

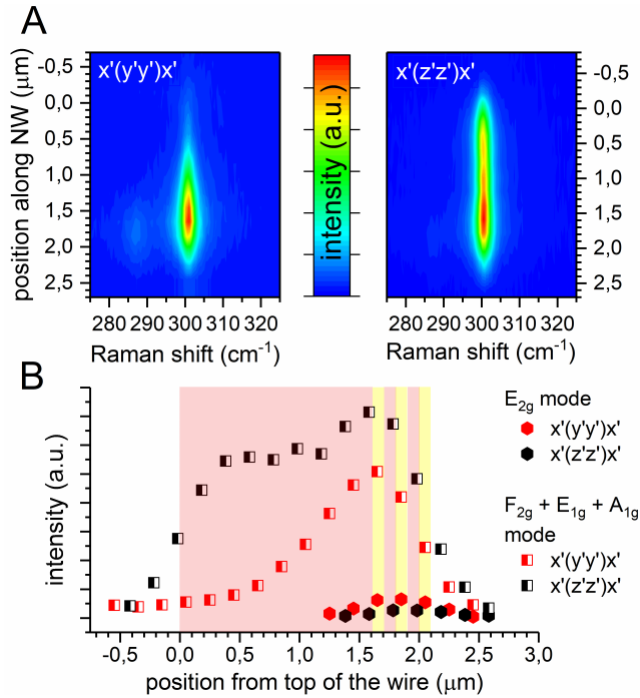


Figure 4. Panel (A): Raman maps as a function of the position along the NW in $x'(y'y')\bar{x}'$ (left) and $x'(z'z')\bar{x}'$ (right) configurations. Each color plot has been normalized to its maximum intensity. The E_{2g} mode is evident at the bottom of the NW, particularly in $x'(y'y')\bar{x}'$ configuration. The intensity of the $F_{2g}+E_{1g}+A_{1g}$ peak is rather homogeneous in $x'(z'z')\bar{x}'$, whereas in $x'(y'y')\bar{x}'$ decreases in the untransformed top part of the wire. Panel (B): extracted intensity of the E_{2g} mode (hexagonal phase, filled hexagons) and of the convoluted F_{2g} (cubic), E_{1g} , and A_{1g} (hexagonal) non-resolved modes (half-filled squares) estimated by Lorentzian fitting, as a function

of the position along the NW. Here intensities are displayed without normalization. Colors in the background recall the structural composition of the NW, which is about 2.1 μm in length and exhibits a transformed part of about 0.3 μm . Our spatial resolution (~ 500 nm) is such that the signal is extended over a ~ 3 μm length. As expected, the contribution of the E_{2g} mode is localized on the transformed bottom part of the NW. When looking at the $F_{2g}+E_{1g}+A_{1g}$ mode, the effect of the dielectric mismatch is evident in $x'(y'y')\bar{x}'$, where the intensity detected on the untransformed, thinner part is markedly weaker than detected on the transformed, heterostructured part.

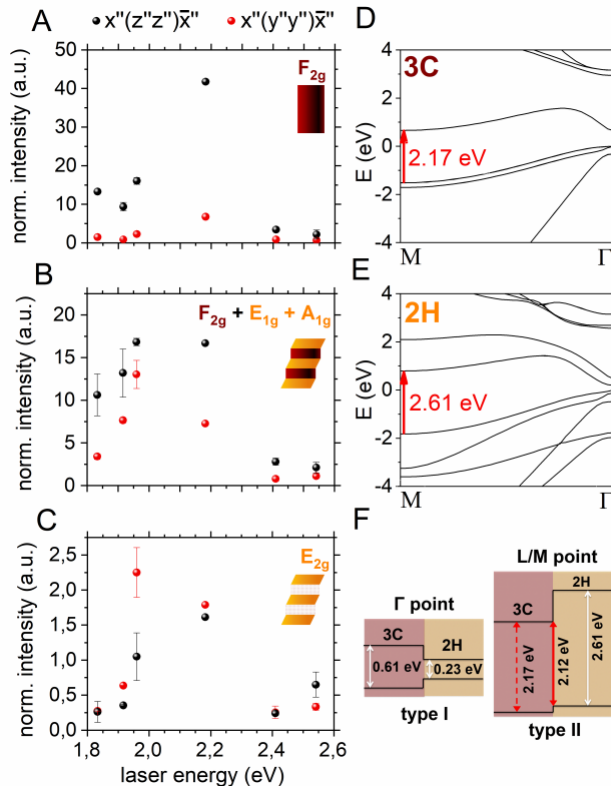


Figure 5. Resonant Raman study performed by monitoring the Raman intensity as the system is excited with different laser energies, covering the whole visible spectrum. We have here studied the modes of the untransformed cubic (F_{2g} mode, panel A) and heterostructured segments ($F_{2g} + E_{1g} + A_{1g}$ mode in panel B, E_{2g} mode in panel C). The Raman intensity of the diamond phase, measured on the untransformed part of the NW, is clearly peaked around 2.2 eV. The intensity detected on the heterostructured part of the NW is instead peaked at lower energies, between 2.0 and 2.2 eV. The bandstructure diagrams for 3C- and 2H-Ge calculated within HSE06-DFT and including spin-orbit coupling are shown in panels D and E, respectively; energies are referred to

the top of the valence band. In panel F the calculated band alignment in the hexagonal-cubic heterostructure is shown. The M point of the hexagonal BZ is equivalent to the L point of the cubic BZ (see e.g. the discussion in Murayama et al. [64]). The transition responsible for the resonant Raman behavior according to Cerdeira et al.⁴⁵ is highlighted (dashed red arrow). The type-II alignment at the L/M point opens a new channel for electronic excitation that is compatible with our resonant experimental observations (solid red arrow). The band offset at the interface was calculated by the average potential method,^{71,72} which relies on the alignment of the vacuum level of two independent slab calculations of the two phases.

ASSOCIATED CONTENT

Supporting Information. A detailed description of the calculations of Raman selection rules and Raman spectroscopy analysis is given in the Supporting Information. The computational methods are presented in detail. (PDF)

AUTHOR INFORMATION

Corresponding Author

*Email: claudia.fasolato@unibas.ch

*Email: ilaria.zardo@unibas.ch

Present Addresses

⊥ Dipartimento di Fisica e Geologia, Università di Perugia, Via Alessandro Pascoli, I-06123 Perugia, Italy

⊥ Email: claudia.fasolato@unipg.it

Orcid

Claudia Fasolato: 0000-0003-3450-404X; Laetitia Vincent: 0000-0002-9813-9259; Riccardo Rurali: 0000-0002-4086-4191; Ilaria Zardo: 0000-0002-8685-2305.

Author Contributions

I.Z. and L.V. conceived the experiment. C.F., M.D.L., D.D., G.D.I., and V.P. performed the Raman measurements. C.F. analyzed the experimental results. C.R. and D.D. grew the nanowires and prepared the samples. L.V. acquired the TEM images. R.R., M.A., and C.F. performed the theoretical calculations. C.F., M.D.L., and I.Z. wrote the manuscript. All authors discussed the results and commented on the manuscript. All authors have given approval to the final version of the manuscript.

Acknowledgments

I.Z. acknowledges financial support from the Swiss National Science Foundation research grant (Project Grant No. 200021_165784). C.F. acknowledges financial support from Sapienza University scholarship “Borsa di Perfezionamento all’Estero 2017-2018”. R.R. acknowledges financial support by the Ministerio de Economía, Industria y Competitividad (MINECO) under grant FEDER-MAT2017-90024-P and the Severo Ochoa Centres of Excellence Program under Grant SEV-2015-0496 and by the Generalitat de Catalunya under grants no. 2017 SGR 1506. L.V. acknowledges financial support from the IDEX Paris-Saclay (ANR-11-IDEX-0003-02). This work was partly supported by the ANR HEXSIGE project (ANR-17-CE030-0014-01) of the French Agence Nationale de la Recherche. R.R. and M.A. thank Giacomo Giorgi and Thanayut Kaewmaraya for useful discussions.

Notes

The authors declare no competing financial interest.

REFERENCES

1. Caroff, P.; Bolinsson, J.; Johansson, J. Crystal phases in III-V nanowires: From random toward engineered polytypism. *IEEE J. Sel. Top. Quantum Electron.* **2011**, *17*, 829–846.
2. Krogstrup, P.; Jorgensen, H. I.; Johnson, E.; Madsen, M. H.; Sorensen, C. B.; Fontcuberta i Morral, A.; Aagesen, M.; Nygard, J.; Glas, F. Advances in the theory of III-V nanowire growth dynamics. *J. Phys. D: Appl. Phys.* **2013**, *46*, 313001.
3. Bechstedt, F.; Belabbes, A. Structure, energetics, and electronic states of III–V compound polytypes. *J. Phys.: Condens. Matter* **2013**, *25*, 273201.
4. Fontcuberta i Morral, A.; Arbiol, J.; Prades, J. D.; Cirera, A.; Morante, J. R. Synthesis of Silicon Nanowires with Wurtzite Crystalline Structure by Using Standard Chemical Vapor Deposition. *Adv. Mater.* **2007**, *19*, 1347–1351.
5. Hauge, H. I. T.; Verheijen, M. A.; Conesa-Boj, S.; Etzelstorfer, T.; Watzinger, M.; Kriegner, D.; Zardo, I.; Fasolato, C.; Capitani, F.; Postorino, P.; et al. Hexagonal Silicon Realized. *Nano Lett.* **2015**, *15* (9), 5855–5860.
6. Qiu, Y.; Bender, H.; Richard, O.; Kim, M.-S.; Van Besien, E.; Vos, I.; de Potter de ten Broeck, M.; Mocuta, D.; Vandervorst, W. Epitaxial Diamond-Hexagonal Silicon Nano-Ribbon Growth on (001) Silicon. *Sci. Rep.* **2015**, *5*, 12692.
7. Fabbri, F.; Rotunno, E.; Lazzarini, L.; Fukata, N.; Salviati, G. Visible and Infra-red Light Emission in Boron-Doped Wurtzite Silicon Nanowires. *Sci. Rep.* **2014**, *4*, 3603.

8. Shukla, A. K.; Dixit, S. Raman study of phase transformation from diamond structure to wurtzite structure in the silicon nanowires. *J. Phys. D: Appl. Phys.* **2016**, *49*, 285304.
9. Tang, J.; Maurice, J.L.; Fossard, F.; Florea, I.; Chen, W.; Johnson, E.V.; Foldyna, M.; Yu, L.; Roca i Cabarrocas, P. Natural occurrence of the diamond hexagonal structure in silicon nanowires grown by a plasma-assisted vapour–liquid–solid method. *Nanoscale* **2017**, *9*(24), 8113-8118.
10. Vincent, L.; Patriarche, G.; Hallais, G.; Renard, C.; Gardès, C.; Troadec, D.; Bouchier, D. Novel Heterostructured Ge Nanowires Based on Polytype Transformation. *Nano Lett.* **2014**, *14* (8), 4828-4836.
11. Biswas, S.; Doherty, J.; Majumdar, D.; Ghoshal, T.; Rahme, K.; Conroy, M.; Singha, A.; Morris, M. A.; Holmes, J. D. Diameter-Controlled Germanium Nanowires with Lamellar Twinning and Polytypes *Chem. Mater.* **2015**, *27*, 3408-3416.
12. Jeon, N.; Dayeh, S. A.; Lauhon, L. J. Origin of Polytype Formation in VLS-Grown Ge Nanowires through Defect Generation and Nanowire Kinking, *Nano Lett.* **2013**, *13*, 3947–3952.
13. Xiao, S.; Pirouz, P. On Diamond-Hexagonal Germanium. *Journal of materials research* **1992**, *7*(6), 1406-1412.
14. Williams, J. S.; Haber, B.; Deshmukh, S.; Johnson, B. C.; Malone, B. D.; Cohen, M. L.; Bradby, J. E. Hexagonal Germanium Formed via a Pressure-Induced Phase Transformation of Amorphous Germanium under Controlled Nanoindentation. *Phys. Status Solidi - Rapid Res. Lett.* **2013**, *7* (5), 355-359.

15. Raffy, C.; Furthmuller, J.; Bechstedt, F. Properties of Hexagonal Polytypes of Group-IV Elements from First-principles Calculations. *Phys. Rev. B* **2002**, 66, 075201.
16. Cartoixà, X. ; Palummo, M. ; Hauge, H. I. T. ; Bakkers, E. P. A. M. ; Rurali, R. Optical Emission in Hexagonal SiGe Nanowires. *Nano Letters* **2017** ,17 (8), 4753-4758.
17. De, A.; Pryor, C. E. Electronic Structure and Optical Properties of Si, Ge and Diamond in the Lonsdaleite Phase. *J. Phys.: Condens. Matter* **2014**, 26, 045801.
18. Dixit, S.; Shukla, A.K. Optical properties of lonsdaleite silicon nanowires: A promising material for optoelectronic applications. *Journal of Applied Physics* **2018**, 123(22), 224301.
19. Dick, K. A.; Thelander, C.; Samuelson, L.; Caroff, P. Crystal Phase Engineering in Single InAs Nanowires. *Nano Letters* **2010**, 10 (9), 3494-3499.
20. Lehmann, S.; Wallentin, J.; Jacobsson, D.; Deppert, K.; Dick, K. A. A General Approach for Sharp Crystal Phase Switching in InAs, GaAs, InP, and GaP Nanowires Using Only Group V Flow. *Nano Letters* **2013**, 13 (9), 4099-4105.
21. Bouwes Bavinck, M.; Jöns K. D.; Zieliński, M.; Patriarche, G.; Harmand, J.-C. ; Akopian N.; Zwiller, V. Photon Cascade from a Single Crystal Phase Nanowire Quantum Dot. *Nano Letters* **2016**, 16 (2), 1081-1085.
22. Amato, M.; Kaewmaraya, T.; Zobelli, A.; Palummo, M.; Rurali, R. Crystal Phase Effects in Si Nanowire Polytypes and Their Homojunctions. *Nano letters* **2016**, 16 (9), 5694-5700.

23. Rödl, C.; Sander, T.; Bechstedt, F.; Vidal, J.; Olsson, P.; Laribi, S.; Guillemoles, J.-F. Wurtzite Silicon as a Potential Absorber in Photovoltaics: Tailoring the Optical Absorption by Applying Strain. *Phys. Rev. B* **2015**, *92*, 045207.
24. Raya-Moreno, M. ; Aramberri, H.; Seijas-Bellido, J. A.; Cartoixà, X.; Rurali, R. Thermal conductivity of hexagonal Si and hexagonal Si nanowires from first-principles. *Applied Physics Letters* **2017**, *111* (3), 032107.
25. Swinkels, M. Y.; Zardo, I. J. *Phys. D: Appl. Phys.* **2018** in press <https://doi.org/10.1088/1361-6463/aad2>
26. Assali, S.; Gagliano, L.; Oliveira, D. S.; Verheijen, M. A.; Plissard, S. R.; Feiner, L. F.; Bakkers, E. P. A. M. Exploring Crystal Phase Switching in GaP Nanowires. *Nano Letters* **2015**, *15* (12), 8062-8069.
27. Belabbes, A.; Panse, C.; Furthmüller, J.; Bechstedt, F. Electronic bands of III-V semiconductor polytypes and their alignment. *Phys. Rev. B* **2012**, *86*, 075208.
28. Kaewmaraya, T.; Vincent, L.; Amato, M. Accurate Estimation of Band Offsets in Group IV Polytype Junctions: A First-Principles Study. *J. Phys. Chem. C* **2017**, *121* (10), 5820–5828.
29. De Luca, M. ; Polimeni, A. Electronic properties of wurtzite-phase InP nanowires determined by optical and magneto-optical spectroscopy. *Appl. Phys. Rev.* **2017**, *4*, 041102.

30. Senichev, A.; Corfdir, P.; Brandt, O.; Ramsteiner, M.; Breuer, S.; Schilling, J.; Geelhaar, L.; Werner, P. Electronic properties of wurtzite GaAs: A correlated structural, optical, and theoretical analysis of the same polytypic GaAs nanowire. *Nano Res.* **2018**, <https://doi.org/10.1007/s12274-018-2053-5>.
31. Hauge, H. I. T.; Verheijen, M. A.; Conesa-Boj, S.; Etzelstorfer, T.; Watzinger, M.; Kriegner, D.; Zardo, I.; Fasolato, C.; Capitani, F.; Postorino, P.; Kölling, S.; Li, A.; Assali, S.; Stangl, J.; Bakkers, E. P. A. M. Hexagonal Silicon Realized, *Nano Letters* **2015**, 15 (9), 5855-5860.
32. Hauge, H. I. T.; Conesa-Boj, S.; Verheijen, M. A.; Koelling, S.; Bakkers, E. P. A. M. Single-Crystalline Hexagonal Silicon-Germanium. *Nano Lett.* **2017**, 17, 85-90.
33. Vincent, L.; Djomani, D.; Fakfakh, M.; Renard, C.; Belier, B.; Bouchier D.; and Patriarche, G. Shear-driven phase transformation in silicon nanowires. *Nanotechnology* **2018**, 29 (12), 125601.
34. De Luca, M.; Zardo, I. (2017) "Semiconductor Nanowires: Raman Spectroscopy Studies", "Raman Spectroscopy and Applications", Dr. Khan Maaz (Ed.), InTech.
35. A. Cantarero. Review on Raman scattering in semiconductor nanowires: I. theory. *J. Nanophotonics* **2013**, 7(1), 071598.
36. Zardo, I.; Conesa-Boj, S.; Peiro, F.; Morante, J. R.; Arbiol, J.; Uccelli, E.; Abstreiter, G.; Fontcuberta i Morral, A. Raman Spectroscopy of Wurtzite and Zinc-Blende GaAs Nanowires: Polarization Dependence, Selection Rules, and Strain Effects. *Phys. Rev. B* **2009**, 80 (24), 245324.

37. Möller, M.; de Lima, M. M.; Cantarero, A.; Dacal, L. C. O.; Madureira, J. R.; Iikawa, F.; Chiaramonte, T.; Cotta, M. A. Polarized and Resonant Raman Spectroscopy on Single InAs Nanowires. *Phys. Rev. B* **2011**, 84 (8), 085318.
38. Livneh, T.; Zhang, J.; Cheng, G.; Moskovits, M. Polarized Raman Scattering from Single GaN Nanowires. *Phys. Rev. B* **2006**, 74 (3), 035320.
39. Lopez, F. J.; Hemesath, E. R.; Lauhon, L. J. Ordered Stacking Fault Arrays in Silicon Nanowires. *Nano Lett.* **2009**, 9 (7), 2774-2779.
40. Nemeth, P.; Garvie, L. A. J.; Aoki, T.; Dubrovinskaia, N.; Dubrovinsky, L.; Buseck, P. R. Lonsdaleite Is Faulted and Twinned Cubic Diamond and Does Not Exist as a Discrete Material. *Nat. Commun.* **2014**, 5, 5447.
41. Ketterer, B.; Heiss, M.; Uccelli, E.; Arbiol, J.; Fontcuberta I i Morral, A. Untangling the Electronic Band Structure of Wurtzite GaAs Nanowires by Resonant Raman Spectroscopy. *ACS Nano* **2011**, 5 (9), 7585-7592.
42. Zardo, I.; Yazji, S.; Hörmann, N.; Hertenberger, S.; Funk, S.; Mangialardo, S.; Morkötter, S.; Koblmüller, G.; Postorino, P.; Abstreiter, G. $E_1(A)$ Electronic Band Gap in Wurtzite InAs Nanowires Studied by Resonant Raman Scattering. *Nano Lett.* **2013**, 13 (7), 3011-3016.
43. Funk, S.; Li, A.; Ercolani, D.; Gemmi, M.; Sorba, L.; Zardo, I. Crystal Phase Induced Bandgap Modifications in AlAs Nanowires Probed by Resonant Raman Spectroscopy. *ACS Nano* **2013**, 7 (2), 1400-1407.

44. Weinstein, B. A.; Cardona, M. Resonant First- and Second-Order Raman Scattering in GaP. *Phys. Rev. B* **1973**, 8 (6), 2795-2809.
45. Cerdeira, F.; Dreybrodt, W.; Cardona, M. Resonant Raman Scattering in Germanium. *Solid State Commun.* **1972**, 10, 591–595.
46. Wieser, N.; Ambacher, O.; Felsl, H. P.; Görgens, L.; Stutzmann, M. Compositional fluctuations in GaInN/GaN double heterostructures investigated by selectively excited photoluminescence and Raman spectroscopy. *Applied Physics Letters* **1999**, 74 (26), 3981-3983.
47. Yoshikawa, M.; Wagner, J.; Obloh, H.; Kunzer, M.; Maier, M. Resonant Raman scattering from buried Al_xGa_{1-x}N ($x \leq 0.17$) layers in (Al, Ga, In)N heterostructures. *Journal of Applied Physics* **2000**, 87 (6), 2853-2856.
48. Maultzsch, J.; Reich, S.; Goñi, A. R.; Thomsen, C. Resonant Raman scattering in GaAs induced by an embedded InAs monolayer. *Phys. Rev. B* **2000**, 63, 033306.
49. Paillard, V.; Puech, P.; Laguna, M. A.; Resonant Raman scattering in polycrystalline silicon thin films. *Appl. Phys. Lett.* **1998**, 73, 1718.
50. Lemos, V.; Silveira, E.; Leite, J. R.; Tabata, A.; Trentin, R.; Scolfaro, L. M. R.; Frey, T.; As, D. J.; Schikora, D.; Lischka, K. Evidence for Phase-Separated Quantum Dots in Cubic InGaN Layers from Resonant Raman Scattering. *Phys. Rev. Lett.* **2000**, 84, 3666.

51. Xu, T.; Nys, J. P.; Addad, A.; Lebedev, O. I.; Urbieto, A.; Salhi, B.; Berthe, M.; Grandidier, B.; Stiévenard, D. Faceted Sidewalls of Silicon Nanowires: Au-Induced Structural Reconstructions and Electronic Properties. *Phys. Rev. B* **2010**, 81 (11), 115403.
52. Boukhicha, R.; Gardès, C.; Vincent, L.; Renard, C.; Yam, V.; Fossard, F.; Patriarche, G.; Jabeen, F.; Bouchier, D. Gold Anchoring on Si Sawtooth Faceted Nanowires. *Europhys. Lett.* **2011**, 95 (1), 18004.
53. Arguello, C. A.; Rousseau, D. L.; Porto, S. P. S. First-Order Raman Effect in Wurtzite-Type Crystals. *Phys. Rev.* **1969**, 181 (3), 1351-1363.
54. Loudon, R. The Raman Effect in Crystals; *Advances in Physics*, **1964**, 13, 423-482.
55. Schomacker, K. T.; Delaney, J. K.; Champion, P. M. Measurements of the Absolute Raman Cross Sections of Benzene. *J. Chem. Phys.* **1986**, 85 (8), 42404247.
56. Kallel, H.; Arbouet, A.; Carrada, M.; Assayag, G. B.; Chehaidar, A.; Periwal, P.; Baron, T.; Normand, P.; Paillard, V. Photoluminescence enhancement of silicon nanocrystals placed in the near field of a silicon nanowire. *Phys. Rev. B* **2013**, 88, 081302(R).
57. De Luca, M.; Zilli, A.; Fonseka, A.; Mokkalapati, S.; Miriametro, A.; Tan, H.; Smith, L.; Jagadish, C.; Capizzi, M.; Polimeni, A. Polarized Light Absorption in Wurtzite InP Nanowire Ensembles. *Nano Letters* **2015**, 15, 998.
58. Lopez, F. J.; Hyun, J. K.; Givan, U.; Kim, I. S.; Holsteen, A. L.; Lauhon, L. J. Diameter and Polarization-Dependent Raman Scattering Intensities of Semiconductor Nanowires. *Nano Letters* **2012**, 12 (5), 2266-2271.

59. Fréchette, J.; Carraro, C. Diameter-dependent modulation and polarization anisotropy in Raman scattering from individual nanowires. *Phys. Rev. B* **2006**, 74, 161404(R).
60. Cao, L.; Nabet, B.; Spanier, J. E. Enhanced Raman Scattering from Individual Semiconductor Nanocones and Nanowires. *Phys. Rev. Lett.* **2006**, 96, 157402.
61. Lopez, F. J.; Hyun, J. K.; Givan, U.; Kim, I. S.; Holsteen, A. L.; Lauhon, L. J. Diameter and Polarization-Dependent Raman Scattering Intensities of Semiconductor Nanowires. *Nano Letters* **2012**, 12 (5), 2266-2271.
62. Phan-Huy, M. C.; Moison, J. M.; Levenson, J. A.; Richard, S.; Mélin, G.; Douay, M.; Quiquempois, Y. Surface roughness and light scattering in a small effective area microstructured fiber. *Journal of Lightwave Technology* **2009**, 27 (11), 1597-1604.
63. Yu, P. Y.; Cardona, M. *Fundamentals of Semiconductors: Physics and Materials Properties*. Springer, **2005**.
64. Murayama, M.; Nakayama, T. Chemical Trend of Band offsets at Wurtzite/zinc-blende Heterocrystalline Semiconductor Interfaces. *Phys. Rev. B* **1994**, 49, 4710-4724.
65. Gonze, X.; Vigneron, J. P. Density-Functional Approach to Nonlinear-Response Coefficients of Solids. *Phys. Rev. B* **1989**, 39 (18), 13120-13128.
66. Gonze, X.; Amadon, B.; Anglade, P. M.; Beuken, J. M.; Bottin, F.; Boulanger, P.; Bruneval, F.; Caliste, D.; Caracas, R.; Côté, M.; et al. ABINIT: First-Principles Approach to Material and Nanosystem Properties. *Comput. Phys. Commun.* **2009**, 180 (12), 2582-2615.

67. Veithen, M.; Gonze, X.; Ghosez, P. Nonlinear Optical Susceptibilities, Raman Efficiencies, and Electro-Optic Tensors from First-Principles Density Functional Perturbation Theory. *Phys. Rev. B* **2005**, 71 (12).
68. Hafner, J. Ab-initio Simulations of Materials using VASP: Density-functional Theory and beyond. *J. Comput. Chem.* **2008**, 29, 2044-2078.
69. Heyd, J.; Scuseria, G. E.; Ernzerhof, M. Hybrid Functionals based on a Screened Coulomb Potential. *J. Chem. Phys.* **2003**, 118, 8207.
70. Perdew, J. P., Burke, K. Ernzerhof, M. Generalized Gradient Approximation Made Simple, *Phys. Rev. Lett.* **1996**, 77, 3865.
71. Baldereschi, A.; Baroni, S.; Resta, R.; *Phys. Rev. Lett.* **1988**, 61, 734.
72. Colombo, L.; Resta, R.; Baroni, S.; *Phys. Rev. B* **1991**, 44, 5572.